VECTOR GRAPHS, PHASE TRAJECTORIES AND PORTRAITS OF MAGNETIC FIELD AND SOLAR PLASMA PARTICLE VELOCITIES IN THE HELIOSPHERE PHASE SPACE

J.A. Antonov[a], V.I. Zakharov[a,b,c], I.N. Myagkova[d], N.A. Suhareva*[a,d], J.S. Shugai [d]

[a]*Lomonosov Moscow State University, Moscow, Russia*
[b]*Institute of Atmospheric Physics named after A.M. Obukhov RAS, Moscow, Russia*
[c]*Schmidt Institute of Physics of the Earth of the Russian Academy of Sciences, Moscow, Russia*
[d]*Skobeltsyn Institute of Nuclear Physics Lomonosov Moscow State University, Moscow, Russia*
**e-mail: suhareva@phys.msu.ru*

Received March 04, 2024
Revised April 24, 2024
Accepted May 01, 2024

Abstract. The material presented in the paper continues a series of studies on the development of the use of the vector graph method for analyzing the characteristics of complex field and plasma structures generated by the Sun in interplanetary space. With a simplified approach to describing such systems using statistical methods, the collective processes of plasma and field interactions may remain undetected, in particular, complex multicomponent structures in the spatiotemporal distribution functions may be missed. The main problem of statistical methods is the neglect of the order of the states of the system being studied and the loss of information contained in this order. Based on the data blocks obtained by the detectors of the WIND apparatus in the CWE research complex and provided by the Coordinated Data Analyzes Web database, implementations of graphs for magnetic field induction vectors and solar wind particle velocity vectors reconstructed on the basis of experimental samples are discussed. The regimes of magnetic storms, the formation of magnetic clouds, and events associated with coronal mass ejections, both ICME and CME, are considered. The presented new method of synchronized pairs of graphs allows us to move from a phenomenological description of the process to a classification of the types of observed and studied multi-processes based on the structural implementations of graphs.

Keywords: *interplanetary magnetic field, solar wind, vector graphs, phase trajectories, phase subspaces, magnetic clouds, magnetic storms*

DOI: 10.31857/S00234206250103e4

INTRODUCTION

Solar activity—a key factor in space weather—has a significant impact on our entire planetary system. Among various space weather events, the most energy-intensive and directly affecting Earth and near-Earth space are coronal mass ejections (CMEs), which can accumulate hundreds of millions of tons of solar plasma matter. Enormous clouds of plasma, permeated by the force lines of the Sun's dominant magnetic field, are ejected from the Sun's surface into the surrounding space at speeds of 300–1500 km/s and higher. Typically, the ejection reaches Earth's orbit in 2–3 days [1].

Earth itself also has a powerful magnetic field, and coronal mass ejections, being solar plasma with their own magnetic field, effectively interact with Earth's own magnetic field. The flow of charged particles forming the coronal ejection enters the magnetosphere and leads to compensatory processes that counteract the invading solar plasma flows. The latter manifests in the disturbance of the ring current or auroral region due to the injection of ionospheric current at high latitudes. This circumstance leads to the occurrence of a geomagnetic storm (or a series of substorms depending on the structure of the ejection). The geoeffectiveness of the disturbance depends on many factors and is reflected in the varying intensity of the storm, which can lead to serious problems in electrical equipment operation, navigation and communication failures, poses a danger to spacecraft and, sometimes, to astronauts. Interplanetary coronal mass ejections (ICMEs), formed on the Sun as a result of spontaneous activity in the form of flares and coronal mass ejections (CMEs), are one of the main factors of space weather.

Coronal mass ejections occur in the solar corona, which is very rarefied and is lost against the background of regular radiation from the Sun's "surface." Therefore, the evolution of these phenomena can only be observed using special instruments—coronagraphs, which was implemented in the project of 1975 . *OSO* -7 [2]. Despite the need for space observations and the creation of appropriate equipment, the method of solar coronagraphy is simple, widespread, and allows determining the energetics of a large ejection by the size of the shadowing area after or directly during the eclipse [3]. However, this observation method does not allow measuring the concentration and composition of the solar plasma cloud, or its magnetic field. This task was solved with the creation of specialized devices that determine these parameters along with conducting coronagraphic studies of the Sun.

As an example, we can cite the International Solar-Terrestrial Physics program, which aims to study the interaction of the solar wind with Earth's magnetic field. Within the project, two spacecraft were launched: *Wind* and *Pola r,* named according to the regions of near-Earth space in which they were to conduct research — the solar wind region and the polar region. The first spacecraft, data from which is used in this work, was placed at the Lagrange point *L* 1 [4, 5]. On the *Wind* spacecraft, to measure the concentration, energy, and velocity of ions and electrons in the solar wind zone and shock wave, two Faraday cylinders were installed as part of the SWE instrument — a device for analyzing the ion distribution function at 30 energy levels in the range from 150 eV to 8 keV, with up to 20 angular readings per charge cell every 92 s. Each sensor had a 15° inclination to the rotation plane of the *Wind* spacecraft. The circular aperture limited aberration effects near the modulator grid and determined the collection area of the collector plates.

The experiment with the magnetic field on *Wind* provided data for studying a wide range of structure scales and fluctuation characteristics of the interplanetary magnetic field. The main research instrument (MFI) was a dual three-axis fluxgate magnetometer mounted on an extended boom, which provided nominally one vector of field measurements every 92 s. The instrument had a wide dynamic measurement range from ±4 to ±65536 nT for each axis in eight discrete ranges, with errors in the corresponding measurement range from 0.001 to 16 nT [6]. The upper range allowed for complete testing in Earth's field.

The purpose of this work is to develop the author's approach to constructing and analyzing vector graphs as applied to the magnetic field and velocity components of solar wind particles. Compared to coronagraphy, the data obtained in the *Wind* experiment allow us to examine the dynamics of coronal mass ejection parameters passing through the spacecraft's location point. When using graph theory methods with synchronization, the data provide an opportunity to identify and visualize the dynamics of joint variations in the magnetic field and velocities of particles participating in the observed event. As far as known, joint processing of coronal ejection parameters has not been conducted before, but it will allow for deeper investigation and interpretation of collective processes occurring in the magnetic and kinetic subsystems of the heliosphere, including reliably noting transitions between states of these subsystems.

PHASE TRAJECTORIES AND PHASE PORTRAITS

The interplanetary magnetic field in interaction with solar wind plasma flows represents a complex stochastic open system, the evolution of which is determined by many external and internal factors, primarily the solar wind particle flux, energetics, and directional pattern of cosmic rays. The subject of this research is the spatial-temporal structure of the interplanetary magnetic field, the dynamics of which is largely related to the solar wind. The non-stationarity, inhomogeneity, and anisotropy of spatial probability distributions for the values of magnetic field components and external acting factors practically exclude the application of the classical apparatus of non-equilibrium statistical mechanics to describe such systems. Open nonlinear dynamical systems typically exhibit collective or group processes initiated by the inhomogeneity and anisotropy of the spatial energy distribution; non-stationarity and inhomogeneity of temperature characteristic concentrations. As a result of nonlinear interaction in these processes, deep memory and spatial long-range action are formed in the system under study. Creating multi-parameter models of such systems belongs to tasks of high complexity level, solved under simplifications with forced hierarchy of processes occurring in the system [7-10]. The search for solutions in classical phase space or in generalized phase space is promising for such tasks.

The classical phase space uses two types of coordinates - spatial and momentum, and preserves the phase volume for conservative Hamiltonian systems. Since the processes under consideration are dissipative, it is necessary to move to a generalized phase space that operates with higher-order kinematic variables. Let us define a finite-dimensional metric space Ω, whose elements are vectors $\vec{\xi} = \left\{\vec{r}, \vec{v}, \dot{\vec{v}}, \ldots\right\}^T$ .In the space Ω, let us consider a physical system consisting of N kinematic points. Each kinematic point of the system can be associated with a cell of the generalized phase space at a given moment of time t . After adding the time axis T to Ω, we obtain Ω_T, which we will call the generalized phase space-time. Let us select a time interval for analyzing the kinematics of the system, assuming that the system of dynamic equations, the time reference point $t_0 \in T$ and the initial state $\vec{\xi} = \left\{\vec{r}_0, \vec{v}_0, \dot{\vec{v}}_0, \ldots\right\}^T \in \Omega$. are known. As a result, we define the profile of the generalized phase trajectory as follows:

$$\vec{\xi}(t) = \left\{\vec{r}(t), \vec{v}(t), \dot{\vec{v}}(t), \ldots\right\}^T . \quad (1)$$

It should be noted that in the generalized phase trajectory, all vector quantities are dependent, which in some cases allows us to exclude time and move to a phase portrait:

$$\vec{v}_0 = \left.\frac{d\vec{r}}{\mathrm{dt}}\right|_{\mathrm{t=t_0}}, \dot{\vec{v}}_0 = \left.\frac{d\vec{v}}{\mathrm{dt}}\right|_{\mathrm{t=t_0}} = \left.\frac{d^2\vec{r}}{\mathrm{dt}^2}\right|_{\mathrm{t=t_0}} . \quad (2)$$

We also note some important properties of phase trajectories that allow us to track unacceptable states and configurations:

- A generalized phase trajectory does not exist for every physical system;
- Only one phase trajectory passes through each point of the generalized space with continuous time;
- Generalized phase trajectories in a space where series of kinematic variables converge do not intersect.

What has been said so far has related to systems that are continuous in time. The situation is different with discrete systems, whose mappings in the form of time series for a combination of scalar and vector quantities are recorded by monitoring equipment. Since this paper discusses vector graphs for vector characteristics, let us discuss the reconstruction of such spatial distributions. Let us define a Cartesian coordinate system whose unit vectors coincide with the unit vectors of the GSE coordinate system.

For a given process model, it is possible to construct a phase trajectory based on a discrete-difference model of the dynamic system. We represent the recorded values of 3D time series samples for the components of the interplanetary magnetic field induction vector and the solar wind plasma velocity vector in the form:

$$B_{i,j,k}[n], V_{i,j,k}[n], \qquad (3)$$

where ijk determines spatial coordinates, n is the number of the cycle.

Time derivatives in discrete representation are replaced by difference ratios, and for the first orders used in this work, they have the form:

$$\Phi_{ijk}[n] = B_{ijk}[n] - B_{ijk}[n-1], \Psi_{ijk}[n] = V_{ijk}[n] - V_{ijk}[n-1]. \quad (4)$$

It is possible to vary the discretization step and synthesize a discrete-difference model of the system under study of arbitrary order. Phase portraits for higher-order kinematic characteristics, which are informative when describing processes with long-range action, deep memory, or collective degrees of freedom, can be synthesized according to a similar scheme.

The developed apparatus of vector graphs includes in the analysis complete information about both the values and the order of implementation sequences. The initial data format is a discretized and quantized multidimensional signal or digital multidimensional signal. The graph is built on the basis of experimental samples for field vector projections $\vec{B}, \vec{V}$ and their combinations. Field vectors converge and diverge at the graph nodes, the graph edges allow controlling the trajectory profile of the system in the phase subspace and reconstructing the transition tree for a specific vector field. By mapping the dependence of the first kinematic variable on the value of the argument - the current value of the field vector, we obtain the desired 3D phase trajectory in the magnetic subspace. Similarly, it is possible to synthesize phase portraits for higher-order kinematic characteristics, which are informative when describing processes with long-range action, deep memory, or collective degrees of freedom.

Selected parameters for graph synthesis:

- data source — the *Wind* spacecraft, located at the libration point L 1;
- analyzed time interval of events — year 2023;
- time series used are presented in the Coordinated Data Analysis Web (CDAWeb) database;
- sampling interval — 60 s,
- quantization step of field induction projections — 0.01 nT (the quantization step is related to sensor accuracy, registration and smoothing methodology, hardware errors of the recorder, overload protection logic);
- quantization step of plasma particle velocity projections — 0.1 nT or 0.1 km/s, depending on the representation;
- count accumulation intervals for graph synthesis — 1440, 5000, 7200, and 32000 cycles. The accumulation time scale determines the target scale for displaying the dynamic process using a graph.

Let's define a scale grid of the 3D phase subspace in which graphs of permissible states of the interplanetary magnetic field are displayed. A node of the scale grid can be a sink or a source in the description of permitted transitions; edges connecting pairs of nodes are generally not limited in length and orientation. The peculiarity of the introduced vector graphs allows two directions of edges between any pair of nodes and the degeneration of nodes, corresponding to the presence of multiple sinks and sources for each of the nodes [11–15].

The transition between discrete samples and continuous description of recorded signals is possible using bilinear transformation or Möbius transformation; linear difference methods cannot be used due to strong systematic errors in such mappings. Henceforth, we will consider the state subspaces of the magnetic and kinetic subsystems as homogeneous and isotropic. The number of available states in the phase subspaces is related to the established upper limit of the observed parameter values and the resolution of the recording device.

COMBINED VECTOR GRAPHS OF MAGNETIC AND KINETIC SUBSYSTEMS

As a rule, the theoretical apparatus for describing the kinematics and dynamics of a nonlinear, non-stationary, and non-equilibrium system operates with a unified phase space in which the physical system under study is analyzed. If such an approach is excessively complex, hierarchical models of splitting the original system into groups of subsystems are used, each of which has its own phase subspace dimension, has its own relaxation time, guaranteeing the transition to equilibrium in the considered subsystems before equilibrium is reached in the system as a whole. Reconstruction of the phase portrait and writing a chain of equations describing the dynamics are equivalent to finding a solution in the selected subspaces.

Another mathematical method for analyzing complex structures in phase space is based on the analysis of marginal projections of the phase portrait onto a set of planes forming a spatial coordinate system. Depending on the correlation characteristics, the degree of spatial coherence, and the geometry of the magnetic field wave structures, a spatio-temporal mapping of probability distributions and their spatial moments from the first to higher orders becomes available. Such mapping has an analogy with the Wigner mapping in phase space for wave beams and pulses and a number of quantum mechanical problems.

The paper uses a third approach, allowing the division of the unified phase space of the heliosphere system under study into two subspaces — the magnetic field and the solar wind plasma. The process of measuring values for the projections of the magnetic field induction vector and the projections of the drift velocity vector of charged solar wind particles is hardware-synchronized by unified measurement timing, and their corresponding graphs can be combined into a time-aligned pair of distributions. Examples of such pairs are presented in Fig. 1.

Fig. 1. Samples of vector graphs of the interplanetary magnetic field (left column) and solar wind particle velocity (right column) for quiet magnetic field (top row) and magnetic storm mode (bottom row)

The top row combines graphs for the magnetic field vector and solar wind particle velocity vector, constructed for a four-day interval from April 15 to 19 April 2023 , corresponding to an undisturbed regime of the interplanetary magnetic field, the spacecraft was in the $\ominus$ sector of the

Sun's magnetic field [16]. The determination of the sector sign was performed based on the analysis of a week-long time series for the B_x *component,* passed through a low-frequency filter with an averaging window of 6000 samples at a discretization step of 60 s. The bottom group of graphs refers to the magnetic storm regime in the interval of April 20-24 April 2023, the spacecraft shifted to the positive sector of the Sun's magnetic field $\oplus$.

The multicomponent structure of the solar wind particle flow complicates the methods of synthesis and analysis of phase trajectories, primarily due to the separation of phase space regions accessible to fast and slow components of the solar wind. In addition to separation in the phase space of kinematic variables of the first, second, and higher orders, each component creates its own phase portrait, determined by the physical processes of mass ejection sources that give rise to magnetic storms, magnetic clouds, as the most common objects of transfer of highly effective disturbances in the heliosphere.

Correct comparison of the structure of several graphs of the same type is possible when aligning the spatial scales of component registration. Simplifying the comparison of quantitative characteristics of reconstructed graphs for the magnetic field is proposed to be performed using a normalized reference surface, which determines the energy scale and orientation of the main axes for the reference surface in ellipsoidal approximation [17]. A different situation develops when selecting dominant orientations for the solar wind particle flow subsystem. Depending on the polarity of the heliosphere's magnetic field, the solar wind particle path takes the form of a spiral with a direction dependent on the polarity of the traversed sector of the Sun's magnetic field. In this case, each component forms its own phase trajectory, combining it with other partial phase trajectories of velocity graphs, creating collective structures during the evolution process.

VECTOR GRAPHS OF MAGNETIC STORMS IN 2023

Let's consider a series of magnetic storms recorded during 2023 and associated with flare activity. When selecting the analyzed processes, two parameters are significant:

- time interval for data capture and analysis;
- absence of significant data loss in the selected interval for both the magnetic field vector components and the plasma particle velocity vector components.

The minimum autocorrelation time from partial time series is typically chosen as the intrinsic time scale in the analysis of phase trajectories and graphs. For highly anisotropic stochastic processes, the intrinsic times of different components of a composite time series may differ or change as new acting factors emerge. Let's consider the properties of the graph in a time interval that significantly exceeds the autocorrelation times and includes no more than 5000 samples with a 60 second interval, which corresponds to a four-day interval. The condition on the proportion of lost records, limited from above by a value of 0.15, is met for 4 events, two in the first and two in the second half of 2023 year. The location of the selected intervals on the year's timeline is [050, 070], [100, 120], [230, 250] and [300, 320].

In Fig. 2 and 3 show images of paired vector graphs, with time intervals indicated in the captions at the top of each graph. Without considering the details of the graph structures, several common features of the synthesized distributions can be identified:

- all observed population density distributions have a dominant orientation along the X axis,
- "accumulative graphs" for the magnetic induction vector in "cross-section" represent a system of quasi-concentric ellipsoids (this image is not shown in the figures, it should be observed during the layer-by-layer synthesis of the graph for the IMF vector);

- graphs for the plasma particle velocity vector are multi-component with areas of "cold" and "hot" zones of the solar wind, the number of areas can be larger, for example, when a magnetic cloud passes through the heliosphere state control zone;
- unlike the reference surface for the vector $\vec{B}$, which has an ellipsoid shape, the profile of the graph for $\vec{V}$ resembles a spiral, the axis of which is close to the X direction. The study of the properties of the reference spiral of the solar wind velocity vector graphs can be performed using the marginal projections method, discussed in the "Dynamic and Statistical Measures of Vector Graphs" section of the article.

In general, vector graphs under magnetic storm conditions have many common structural features that allow assessing the type and geometry of disturbances in the heliosphere state produced by external factors.

Fig. 2. Vector graphs for the first half of 2023 in the day intervals [050, 070] and [100, 120]

Fig. 3. Graphs of vectors for the second half of 2023 in the day intervals [230, 250] and [300, 320]

VECTOR GRAPHS OF MAGNETIC CLOUDS IN THE FIRST HALF OF 2023

A number of works are devoted to the study of magnetic clouds and their connection with ICMEs [18, 19], investigating the geoeffectiveness of such structures, their role in the formation of storm events [20-22], and creating dynamic and statistical models that allow predicting the stages of origin, development, and destruction of magnetic clouds in interplanetary space [23, 24]. In this paper, we consider a set of events related to the formation of magnetic clouds and their accompanying structures. Episodes of the analyzed process were selected from catalogs [25, 26] with an update date of February 1, 2024. Table 1 shows the time of disturbance registration that generated the event, the start time, and the end time of the observed event. In addition to the temporal parameters obtained from observations, a qualitative typification of events is used based on the correspondence of the process development to the magnetic cloud model [26].

Table 1. List of events from 03.I.2023 to 20.V.2023 related to the magnetic cloud formation process

Disturbance registration, hh:mm	ICME start	ICME end	Type
03.I.2023, 21:00	04.I.2023, 02:00	05.I.2023, 22:00	2
27.II.2023, 10:00	27.II.2023, 20:00	28.II.2023, 17:00	0
01.II.2023, 00:00	01.III.2023, 09:00	01.III.2023, 21:00	1
02.III.2023, 09:00	02.III.2023, 09:00	02.III.2023, 22:00	1
12.III.2023, 06:00	12.III.2023, 09:00	14.III.2023, 02:00	1
15.III.2023, 04:27	15.III.2023, 21:00	17.III.2023, 07:00	0
23.III.2023, 05:00	23.III.2023, 14:00	24.III.2023, 07:00	2
18.IV.2023, 14:02	19.IV.2023, 08:00	21.IV.2023, 02:00	2

23.IV.2023, 17:38	24.IV.2023, 01:00	25.IV.2023, 19:00	2
09.V.2023, 22:50	10.V.2023, 12:00	12.V.2023, 06:00	0
12.V.2023, 06:33	12.V.2023, 12:00	13.V.2023, 21:00	0
20.V.2023, 10:00	20.V.2023, 10:00	21.V.2023, 16:00	1

The rightmost column defines the "distinctiveness" of the magnetic cloud based on registered quantitative parameters using a three-level scale in the presence of an ICME event.

Type 0 — ICME does not generate a magnetic cloud, the forming structure lacks most of the magnetic cloud features, such as slow rotation and local magnetic field enhancement.

Type 1 — ICME shows signs of field direction rotation, but it lacks some other magnetic cloud characteristics, such as field strength enhancement in the magnetic cloud region.

Type 2 — ICME has clear features of a magnetic cloud.

The time intervals indicated in Table 1. contain an unacceptably high percentage of data gaps; to prevent erroneous deformation of vector graphs of both the magnetic field and solar wind, 5 events out of 12 considered were left for analysis. Below are the paired vector graphs of events.

Fig. 4. Type 0 Event. The plasma flow velocity graph did not form due to partial data loss. The magnetic field graph shows multiple fragments of slow rotation.

The graph structures presented in Fig. 4-8 should be considered as a qualitative demonstration of the method's capabilities. A rigorous quantitative approach requires, in addition to hardware synchronization, alignment of the characteristic time scales of magnetohydrodynamic processes in the magnetic and kinetic subsystems. The authors previously conducted an analysis of such characteristics of the magnetic field induction vector components and solar wind particle velocity using topological analysis of time series. A two-fold difference in the intrinsic time scales of the magnetic and kinetic subsystems was revealed [27]. Such time scale corrections may be needed when reconstructing difference or continuous process equations based on the shape of phase portraits, and in no way diminish the significance of graph reconstruction results under conditions of hardware synchronization.

Fig. 5. Type 1 Event. The plasma flow velocity graph did not form due to partial data loss. The magnetic field graph shows pronounced slow rotation of the magnetic field.

Fig. 6. Type 2. All signs of a magnetic cloud are present.

Fig. 7. Type 2. All signs of a magnetic cloud are present.

Fig. 8. Type 2. All signs of a magnetic cloud are present.

DYNAMIC AND STATISTICAL MEASURES OF VECTOR GRAPHS

Quantitative measures of synthesized vector graphs must be consistent with their geometry and provide sufficient information for an unambiguous description of the graph properties and the type of process it corresponds to. Depending on the problem being solved, different sets of vector graph measures are used. Let's consider two types of parameters: **dynamic** , describing the general geometry of the synthesized graph and the laws of its evolution in phase space, and **statistical** , describing the probability density distributions of the phase trajectory passing through graph nodes in a given observation time interval.

Tensor of Population Distribution of Vector Graph Nodes

Let us define quantitative measures for vector graphs reconstructed from experimental samples, based on the graph structure and the corresponding support surfaces of phase portraits or attractors of phase trajectories. For magnetic field vector graphs, tensor methods are physically justified, allowing detailed information about the geometry of the phase portrait in elliptical approximation, the direction of the principal axes, and the invariants of the second rank tensor. We will consider the problem in the GSE coordinate system. The coordinates of each cell in the phase space will be indexed by three values of quantum numbers, determining the interval values of the magnetic field vector projections on the *X,Y,Z* coordinate axes. The population of each graph node is determined by the number of state realizations corresponding to the selected cell — $N_{x,y,z}$, regardless of the direction of passage through each node. Strictly speaking, in addition to the specified metrics for the phase space cells, the values of the initial and final time intervals for the process under study should be considered, introducing summation limits in expression (5).

By analogy with the description of solid body motion, we introduce a second rank tensor for the population of states or nodes I_b [28, 29]:

$$I\widehat{(x,y,z)} = \begin{array}{ccc} (y^2+z^2)\sum\limits_i N_{i,y,z} & -xy\sum\limits_k N_{x,y,k} & -xz\sum\limits_j N_{x,j,z} \\ -xy\sum\limits_k N_{x,y,k} & (x^2+z^2)\sum\limits_j N_{x,j,z} & -yz\sum\limits_i N_{i,y,z} \\ -xz\sum\limits_j N_{x,j,z} & -yz\sum\limits_i N_{i,y,z} & (x^2+y^2)\sum\limits_k N_{x,y,zk} \end{array} . \qquad (5)$$

Here (*i,j,k*) are summation variables; (*x,y,z*) are coordinates of the phase space cell; $N_{x,y,z}$ is the number of realizations for the phase space cell (*x,y,z*).

The diagonal elements of the recorded tensor I_{xx}, I_{yy}, I_{zz} are often called moments with respect to axes *X,Y,Z* . For the analysis of quantitative characteristics of the considered tensor, the property of additivity is important, allowing to distinguish the components of the phase portrait related to parallel processes. The symmetry property of the constructed second-rank population distribution tensor allows its reduction to a diagonal form in the principal axes of the figure under study — X_1, X_2, X_3. The values of tensor components recorded in such axes define the principal moments related to each other by a group of inequalities:

$$I_1 + I_2 \geq I_3, \qquad I_2 + I_3 \geq I_1, \qquad I_1 + I_3 \geq I_2. \qquad (6)$$

In analytical geometry, a classification of analyzed spatial distributions is adopted based on comparing the values of principal moments:

- asymmetric top — $I_1 \neq I_2 \neq I_3 \neq I_1$;
- symmetric top — $I_1 = I_2 \neq I_3$;
- spherical top — $I_1 = I_2 = I_3$.

By operating with the orientation of principal axes and values of principal moments, it is possible to determine a number of quantitative measures related to the symmetry of the analyzed figure, since symmetry properties inherent in the investigated graph should be inherited by its tensor measures.

Marginal Projections for Distribution of Node Populations in a Vector Graph

When working with complex 3D profiles of a vector graph, methods operating with marginal projections of the graph onto a set of planes formed by the GSE coordinate system basis vectors or any additional directions informative for the process under study are effective. Let's consider an example of projection onto planes orthogonal to the X,Y,Z axes, which we define by pairs of basis vectors belonging to them — (YZ) , (XZ) , (XY). Let the distribution of the number of realizations for each node of the registered graph $N_{x,y,z}$ be given, and projection along the direction Z onto the plane (XY) be performed. As a result, we obtain a 2D distribution of the number of realizations in projection onto three selected mutually orthogonal planes:

$$P_Z(x,y)=\sum_k N_{x,y,k}, P_Y(x,z)=\sum_j N_{x,j,z}, P_X(y,z)=\sum_i N_{i,y,z}. \qquad (7)$$

On each of the projection planes, we define the components of the first spatial moment vector for the 2D distribution as follows [30]:

$$M_x^{(1)}=\frac{\Sigma\sum_{ij} iP_z(i,j)}{\Sigma\sum_{ij} P_z(i,j)} \quad (8)$$

$$M_x^{(1)}=\frac{\Sigma\sum_{ij} jP_z(i,j)}{\Sigma\sum_{ij} P_z(i,j)} \qquad (9)$$

Here and further, the introduced metrics will be written only for one projection Z : (XY), distributions for projections Y : XZ) and X : YZ) can be obtained by cyclic permutation of the summation variables. The first spatial moment determines the coordinate values of the geometric center of the node population distribution in the vector graph. The profile of the marginal projection of the population distribution in elliptical or quadratic approximation is described by a symmetric second-rank tensor of the second central spatial moment with components [31]:

$$M_{xx}^{(2)}=\frac{\Sigma\sum_{ij}\left(i-M_x^{(1)}(k)\right)^2 P_z(i,j)}{\Sigma\sum_{i,j} P_z(i,j)} \qquad (10)$$

$$M_{xy}^{(2)}=\frac{\Sigma\sum_{ij}\left(i-M_x^{(1)}(k)\right)\left(j-M_y^{(1)}(k)\right)P_z(i,j)}{\Sigma\sum_{i,j} P_z(i,j)} \qquad (11)$$

$$M_{yy}^{(2)}=\frac{\Sigma\sum_{ij}\left(i-M_y^{(1)}(k)\right)^2 P_z(i,j)}{\Sigma\sum_{i,j} P_z(i,j)} \quad (12)$$

Various combinations of the three parameters of the second spatial moment allow defining a set of metrics for the profile of marginal projections, such as:

- inclination angles of the major axis of the approximating ellipse;

- diameters of the approximating ellipse;
- elongation value;
- eccentricity value.

The tilt angle of the major axis of the approximating ellipse is determined as follows:

$$2\theta = \arctan\left(\frac{2M_{xy}^{(2)}}{M_{xx}^{(2)} - M_{yy}^{(2)}} \right) \qquad (13)$$

For the diameters of the approximating ellipse, the representation through central spatial moments of the second order is valid in the following form:

$$D_{1,2} = 2\sqrt{2}\sqrt{M_{xx}^{(2)} + M_{yy}^{(2)} \pm \operatorname{sign}\left(M_{xx}^{(2)} - M_{yy}^{(2)}\right)\sqrt{\left(M_{xx}^{(2)} - M_{yy}^{(2)}\right)^2 + 4\left(M_{xy}^{(2)}\right)^2}} \qquad (14)$$

The diameters coincide only when the diagonal moments are equal and the off-diagonal moment is zero.

Eccentricity:

$$Ext = \frac{D_1^2 - D_2^2}{D_1^2 + D_2^2} = \operatorname{sign}\left(M_{xx}^{(2)} - M_{yy}^{(2)}\right)\frac{\sqrt{\left(M_{xx}^{(2)} - M_{yy}^{(2)}\right)^2 + 4\left(M_{xy}^{(2)}\right)}}{M_{xx}^{(2)} + M_{yy}^{(2)}} \qquad (15)$$

Elongation:

$$ELong^2 = \frac{D_{max}^2 - D_{min}^2}{D_{max}^2} \qquad (16)$$

$$ELong^2 = 2\frac{\sqrt{\left(M_{xx}^{(2)} - M_{yy}^{(2)}\right)^2 + 4\left(M_{xy}^{(2)}\right)^2}}{M_{xx}^{(2)} + M_{yy}^{(2)} + \sqrt{\left(M_{xx}^{(2)} - M_{yy}^{(2)}\right)^2 + 4\left(M_{xy}^{(2)}\right)^2}} \qquad (17)$$

In addition to the described metrics based on central moments of the second order, central moments of higher orders can be used for the studied 2D marginal projections, including skewness (third order, 9 elements), and kurtosis (fourth order, 16 elements). Quantitative relationships between higher-order moments allow determining not only specific parameters but also the type of implemented statistical distribution. However, it should be kept in mind that precision decreases with increasing order of calculated moments, and systematic errors grow when estimating their ratios.

CONCLUSION

The method of synchronized vector graphs has been applied for the first time for the consistent analysis of the interplanetary magnetic field states and solar wind flow. The structure and complexity of the graph depend on the duration of the sampling of vector field component values, which allows controlling the information capacity of the graph and changing the time resolution value of the studied process for a more comprehensive study of its details. Interpreting the synthesized vector graph as a phase trajectory, and in some cases as a phase portrait, allows employing the apparatus of statistical physics and the theory of dynamical systems [32–35].

Determining the evolutionary equations for the state of the studied system requires synchronous analysis of phase trajectories in the phase subspaces of the magnetic field and solar wind particle flow vectors. However, the discussion of rules for combining discrete phase subspaces continues to this day. Under such conditions, the proposed empirical approach to reconstructing phase trajectories can become a good selection rule for proposed theoretical models. The application of vector graphs is physically justified in problems of reconstructing the dynamics of processes in interplanetary space and is comparable in informative capacity to the phase trajectory of the studied system.

The accuracy of registration and the discretization step of the available primary time series from satellite monitoring are sufficient for the reconstruction of phase trajectories of the magnetic field induction vector and the solar wind particle velocity vector in their corresponding subspaces. The main portion of systematic reconstruction errors is associated with "dropouts" of series values in the used data arrays. Dropout can be synchronous for both vectors, but data losses are mainly observed for $\vec{V}$ components. The selected measures for quantitative description of the structure of vector graphs and their marginal mappings have the same computational complexity, inherited symmetry types from the graph, and, important for the problems being solved, the property of superposition of structural components of the graph node population distribution. This circumstance makes it possible to study the structure of a coronal ejection in detail and puts the prediction of its evolution in interplanetary space on the agenda.

FUNDING

The work was carried out within the framework of the State Assignment "Solar Research, Monitoring and Modeling of the Radiation Environment and Plasma Processes in the Heliosphere and Near-Earth Space", CITIS Number: 122071200023-6, and the State Assignment "Wave Beams and Pulses in Randomly Inhomogeneous and Stratified Media", CITIS Number: 117121890022-8.

REFERENCES

1. *Maiewski E.V., Malova H.V., Popov V.Y., Zelenyi L.M* . Ulysses flyby in theheliosphere: Comparison of the solar wind model with observational data // Universe. 2022. V. 8(6). Art.ID. 324. DOI: 10.3390/universe8060324

2. *Koomen M., Detwiler C., Brueckner G. et al.* White lightcoronagraph in OSO-7 // Applied Optics . 1975. V. 14(3). P. 743–751.

3. *Chikunova G., Dissauer K., Podladchikova T. et al.* Coronal dimmings associated with coronal mass ejections on the solar limb // Astrophysical J. 2020. V. 896(1). Art.ID. 17. DOI: 10.3847/1538-4357/ab9105

4. *Wilson L.B. III, Brosius A.L., Gopalswamy N. et al.* A quarter century of wind spacecraft discoveries // Reviews of Geophysics. 2021. V. 59(2). Art.ID. e2020RG000714. DOI: 10.1029/2020RG000714

5. *Wilson L.B. III.* Wind 2020 senior review proposal. https://wind.nasa.gov/docs/Wind_SR2020_proposal.pdf

6. *Lepping R., Acũna M., Burlaga L. et al* . The wind magnetic field investigation // Space Science Reviews. 1995. 71 . P. 207–229.

7. *Adhikari L., Khabarova O., Zank G.P. et al.* The role of magnetic reconnection–associated processes in local particle acceleration in the solar wind // Astrophysical J. 2019. V. 873(1). Art.ID. 72. DOI: 10.3847/1538-4357/ab05c6

8. *Bale S., Badman S., Bonnell J. et al* . Highly structured slow solar wind emerging from an equatorial coronal hole // Nature. 2019. V. 576(7786). P. 237–242. DOI: 10.1038/s41586-019-1818-7

9. *Alberti T., Consolini G., Carbone V. et al* . Multifractal and chaotic properties of solar wind at MHD and kinetic domains: An empirical mode decomposition approach // Entropy. 2019. V.21(3). Art.ID. 320. DOI: 10.3390/e21030320

10. *Prasad P.K., Gowrisankar A., Saha A . et al* . Dynamical properties and fractal patterns of nonlinear waves in solar wind plasma // Physica Scripta. 2020. V. 95(6). Art.ID. 065603. DOI: 10.1088/1402-4896/ab833c

11. *Godsil C., Royle G.F* . Algebraic graph theory. Part of the book series: Graduate Texts in Mathematics. V. 207. Springer Science & Business Media, 2001.

12. *Kalofolias V* . How to learn a graph from smooth signals // Artificial intelligence and statistics. P. 920–929. PMLR, 2016.

13. *Pal M., Samanta S., Ghorai G.* Modern trends in fuzzy graph theory. Springer, 2020.

14. *Cheng S.-W., Cheong O., Lee T. et al.* Fitting a graph to one-dimensional data // Theoretical Computer Science. 2021. Iss. 867. P. 40–49.

15. *Daitch S.I., Kelner J.A., Spielman D.A.* Fitting a graph to vector data // Proc. 26th Annual International Conference on Machine Learning. Montreal, Canada. 2009. P. 201– 208.

16. *Shugay Y., Slemzin V., Veselovsky I* . Magnetic field sector structure and origins of solar wind streams in 2012 // J. Space Weather and Space Climate. 2014. V. 4. Art.ID. A24.

17. *Antonov Y., Zakharov V., Myagkova I. et al* . Structure and dynamics for graphs of interplanetary magnetic field vectors // Cosmic Research. 2024. V. 62(2). P. 147–161. https://doi.org/10.1134/S0010952523600336

18. *Kilpua E., Isavnin A., Vourlidas A. et al.* On the relationship between interplanetary coronal mass ejections and magnetic clouds // Annales Geophysicae. 2013. V. 31(7). P. 1251–1265.

19. *Shaikh Z.I., Raghav A.N.* Statistical plasma properties of the planar and nonplanar ICME magnetic clouds during solar cycles 23 and 24 // Astrophysical J. 2022. V. 938(2). Art.ID. 146. DOI: 10.3847/1538-4357/ac8f2b

20. *Wu C.-C., Gopalswamy N., Lepping R.P. et al.* Characteristics of magnetic clouds and interplanetary coronal mass ejections which cause intense geomagnetic storms // Terrestrial, Atmospheric & Oceanic Sciences. 2013. V. 24(2).

21. *Ghag K., Sathe B., Raghav A. et al.* Statistical study of geo-effectiveness of planar magnetic structures evolved within ICME's // Universe. 2023. V. 9(8). Art.ID. 350. https://doi.org/10.3390/universe9080350

22. *Thalmann J., Dumbović M., Dissauer K. et al.* Tracking magnetic flux and helicity from the Sun to Earth: Multi-spacecraft analysis of a magnetic cloud and its solar source // Astronomy & Astrophysics. 2023. V. 669. Art.ID. A72. https://doi.org/10.1051/0004-6361/202244248

23. *Manchester W. IV, Kozyra J., Lepri S. et al.* Simulation of magnetic cloud erosion during propagation // J. Geophysical Research: Space Physics. 2014. V. 119(7). P. 5449–5464.

24. *Li L., Chen T., Shen C. et al.* Near-surface atmospheric electric field changes through magnetic clouds via coronal mass ejections // Geoscience Letters. 2023. V. 10(1). Art.ID. 45. https://doi.org/10.1186/s40562-023-00299-2

25. *Cane H., Richardson I* . Interplanetary coronal mass ejections in the near-earth solar wind during 1996–2002 // J. Geophysical Research: Space Physics. 2003. V. 108(A4).

26. *Richardson I.G., Cane H.V* . Near-earth interplanetary coronal mass ejections during solar cycle 23 (1996–2009): Catalog and summary of properties // Solar Physics. 2010. Iss. 264. P. 189–237.

27. *Antonov J.A., Tsyganov M.V., Suhareva N.A* . Topological properties of satellite monitoring time series for the interplanetary magnetic field // 29th International Symposium on

Atmospheric and Ocean Optics: Atmospheric Physics. Moscow, Russia. 2023. V. 12780. P. 1491–1497. https://doi.org/10.1117/12.2690853

28. *Landau L.D., Lifshits E.M* . Mechanics. V. 1. CUP Archive, 1960.

29. *McConnell A.J* . Applications of tensor analysis. Courier Corporation, 2014.

30. *Goodman J.W* . Statistical optics. John Wiley & Sons, 2015.

31. *Xie C., Zhong W., Mueller K.* A visual analytics approach for categorical joint distribution reconstruction from marginal projections // IEEE Transactions on Visualization and Computer Graphics. 2016. V. 23(1). P. 51–60.

32. *Sadovnikov B., Inozemtseva N., Perepelkin E* . Generalized phase space andconservative systems // Doklady Mathematics. 2013. V. 88. P. 457–459.

33. *Perepelkin E.E., Sadovnikov B.I., Inozemtseva N.G. et al* . Universal density matrix for the phase space // arXiv preprint. 2019. DOI: 10.48550/arXiv.1904.04950

34. *Perepelkin E.E., Sadovnikov B.I., Inozemtseva N.G. et al* . Exact time-dependent solution of the Schroedinger equation, its generalization to the phase space and relation to the gibbs distribution // Physica Scripta. 2022. V. 98(1). Art.ID. 015221.

35. *Perepelkin E.E., Sadovnikov B.I., Inozemtseva N.G. et al* . Dispersion chain of quantum mechanics equations // J. Physics A: Mathematical and Theoretical. 2023. V. 56(14). Art.ID. 145202. DOI:10.1088/1751-8121/acbd71

Figure Captions

Fig. 1: Samples of vector graphs of the interplanetary magnetic field (left column) and solar wind particle velocity (right column) for quiet magnetic field (top row) and magnetic storm mode (bottom row)

Fig. 2. Vector graphs of the first half of 2023 in day intervals [050, 070] and [100, 120]

Fig. 3. Vector graphs of the second half of 2023 in day intervals [230, 250] and [300, 320]

Fig. 4. Type 0 Event. The plasma flow velocity graph did not form due to partial data loss. Multiple fragments of slow rotation are present on the magnetic field graph.

Fig. 5. Type 1 Event. The plasma flow velocity graph did not form due to partial data loss. Pronounced slow rotation of the magnetic field is present on the magnetic field graph.
Fig. 6. Type 2. All signs of a magnetic cloud are present.

Fig. 7. Type 2. All signs of a magnetic cloud are present.

Fig. 8. Type 2. All signs of a magnetic cloud are present.

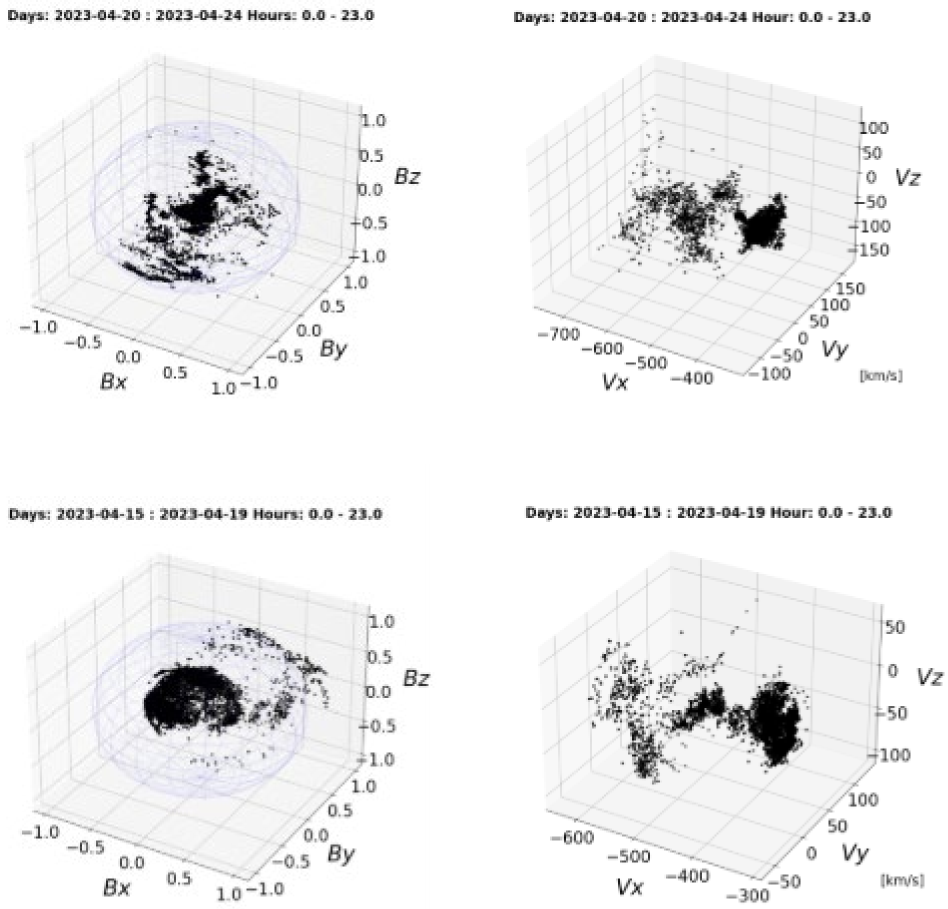
Days: 2023-04-20 : 2023-04-24 Hours: 0.0 - 23.0

Days: 2023-04-20 : 2023-04-24 Hour: 0.0 - 23.0

Days: 2023-04-15 : 2023-04-19 Hours: 0.0 - 23.0

Days: 2023-04-15 : 2023-04-19 Hour: 0.0 - 23.0

Fig. 1

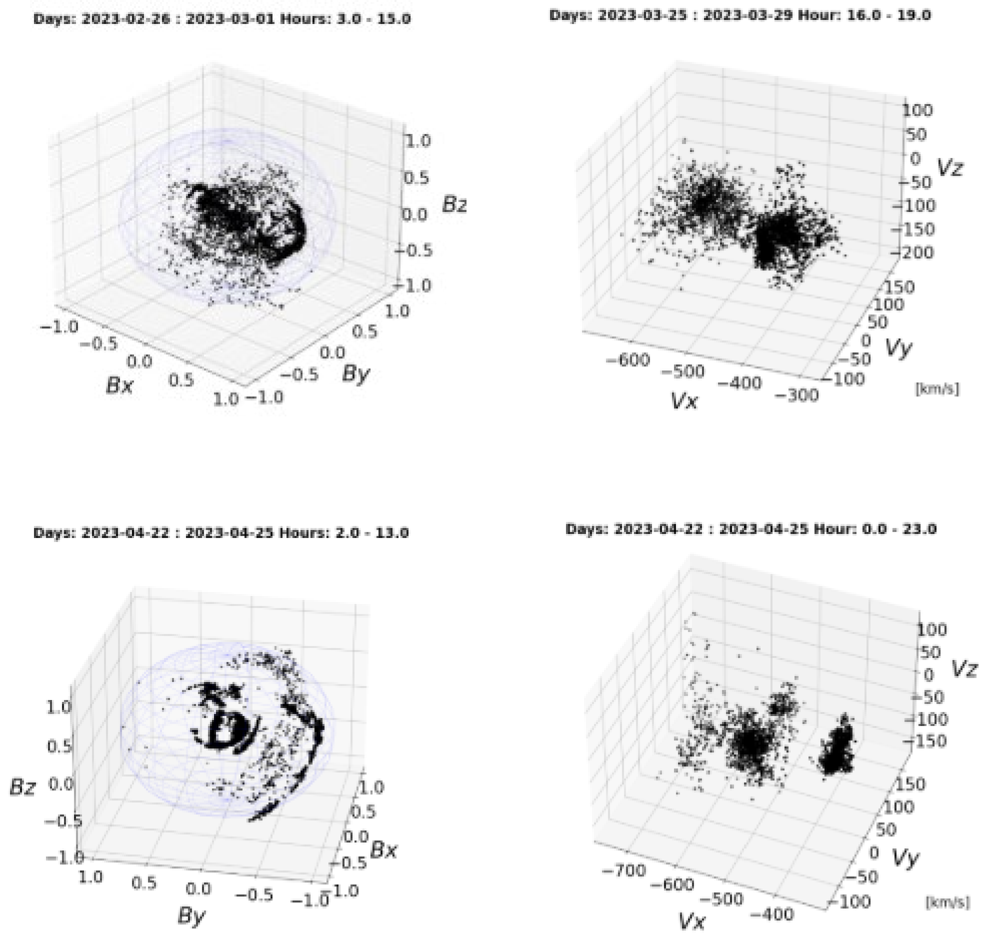
Days: 2023-02-26 : 2023-03-01 Hours: 3.0 - 15.0

Days: 2023-03-25 : 2023-03-29 Hour: 16.0 - 19.0

Days: 2023-04-22 : 2023-04-25 Hours: 2.0 - 13.0

Days: 2023-04-22 : 2023-04-25 Hour: 0.0 - 23.0

Fig. 2

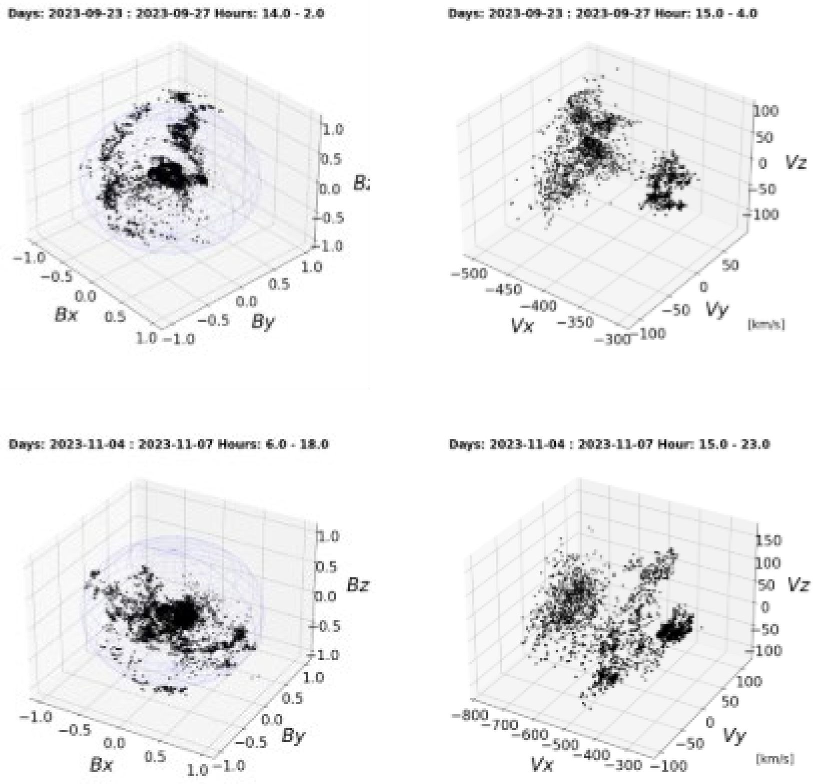

Days: 2023-09-23 : 2023-09-27 Hours: 14.0 - 2.0

Days: 2023-09-23 : 2023-09-27 Hour: 15.0 - 4.0

Days: 2023-11-04 : 2023-11-07 Hours: 6.0 - 18.0

Days: 2023-11-04 : 2023-11-07 Hour: 15.0 - 23.0

Fig. 3

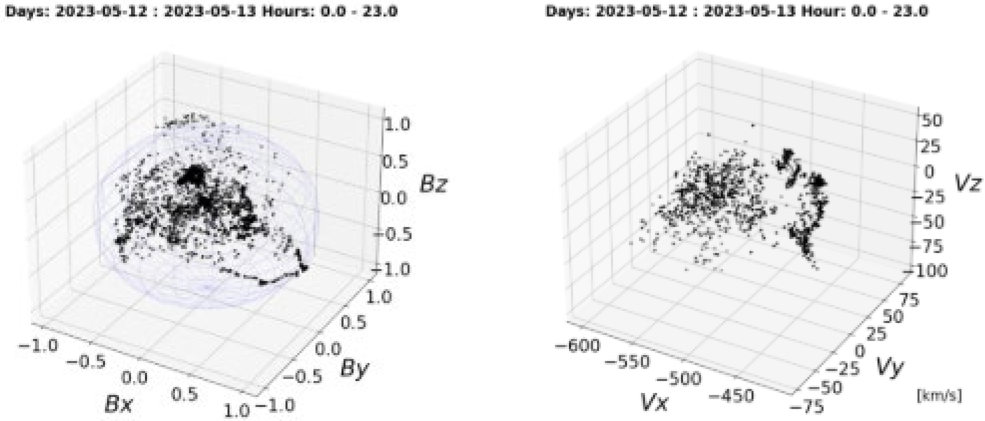
Days: 2023-05-12 : 2023-05-13 Hours: 0.0 - 23.0

Days: 2023-05-12 : 2023-05-13 Hour: 0.0 - 23.0

Fig. 4

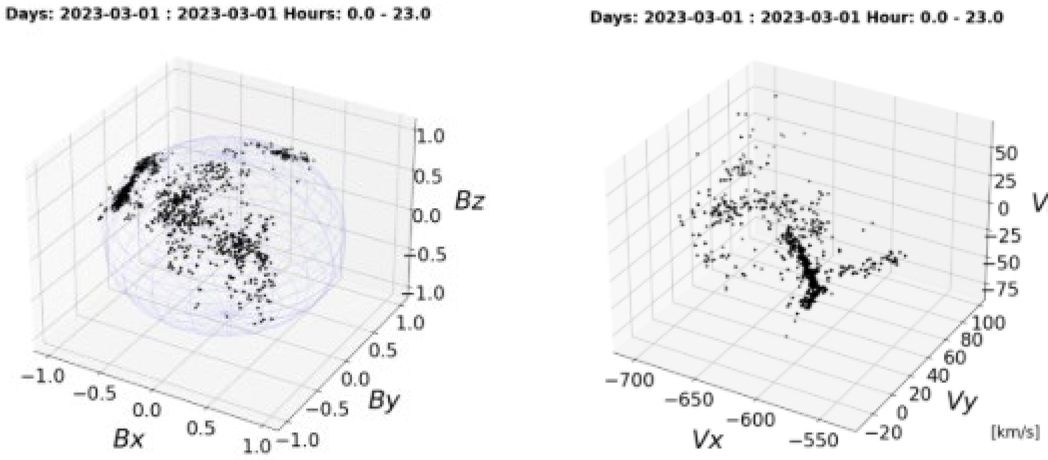

Days: 2023-03-01 : 2023-03-01 Hours: 0.0 - 23.0

Days: 2023-03-01 : 2023-03-01 Hour: 0.0 - 23.0

Fig.5

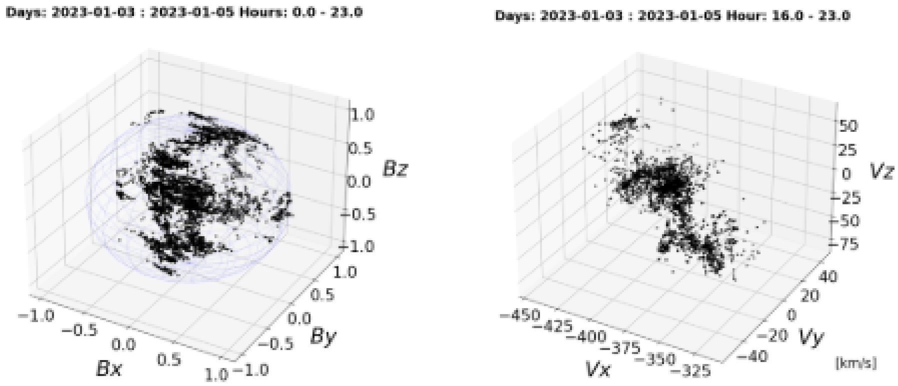
Days: 2023-01-03 : 2023-01-05 Hours: 0.0 - 23.0

Days: 2023-01-03 : 2023-01-05 Hour: 16.0 - 23.0

Fig. 6

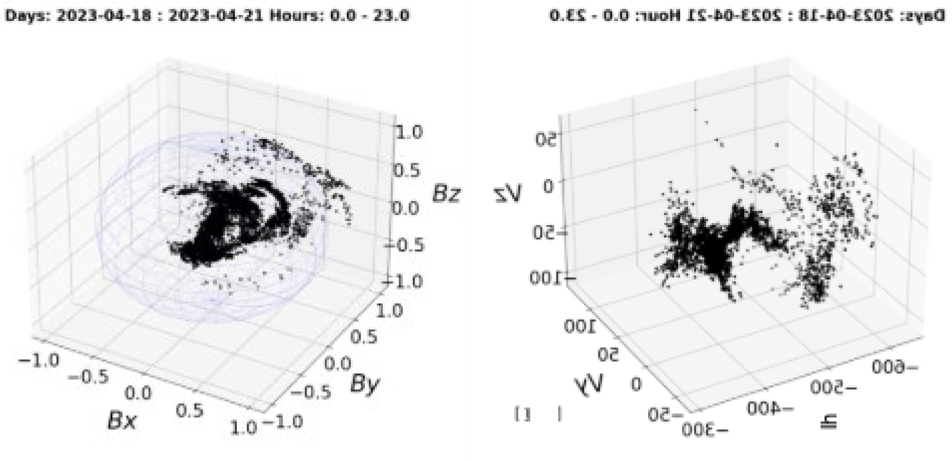
Days: 2023-04-18 : 2023-04-21 Hours: 0.0 - 23.0
Bx
By
Bz
−1.0
−0.5
0.0
0.5
1.0
Days: 2023-04-18 : 2023-04-21 Hour: 0.0 - 23.0
Vz
Vy
50
0
−50
−100
100
−300
−400
−500
−600

Fig. 7

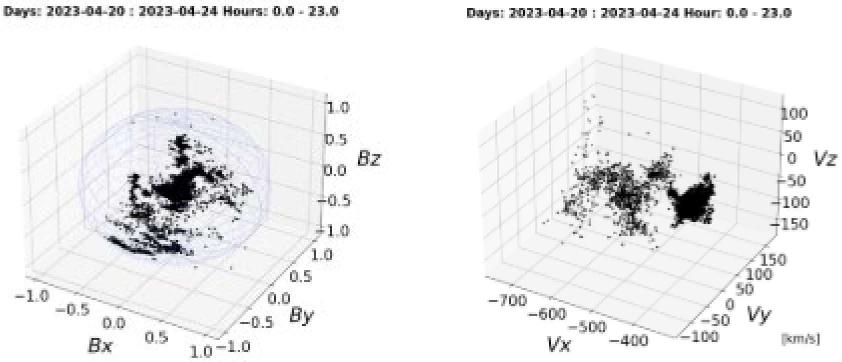
Days: 2023-04-20 : 2023-04-24 Hours: 0.0 - 23.0
Bx
By
Bz
−1.0
−0.5
0.0
0.5
1.0
Days: 2023-04-20 : 2023-04-24 Hour: 0.0 - 23.0
Vx
Vy
Vz
−700
−600
−500
−400
−100
−50
0
50
100
150
[km/s]

Fig. 8